Nano Research 2017, 10(2): 503–519
DOI 10.1007/s12274-016-1309-1
Research Article
ISSN 1998-0124
CN 11-5974/O4

Highly efficient gene silencing and bioimaging based on fluorescent carbon dots *in vitro* and *in vivo*

Seongchan Kim[1,§], Yuri Choi[2,§], Ginam Park[3], Cheolhee Won[3], Young-Joon Park[4], Younghoon Lee[5] (✉), Byeong-Su Kim[2] (✉), and Dal-Hee Min[1,3] (✉)

[1] *Center for RNA Research, Institute for Basic Sciences (IBS), Department of Chemistry, Seoul National University, Seoul 08826, Republic of Korea*
[2] *Department of Energy Engineering and Department of Chemistry, Ulsan National Institute of Science and Technology (UNIST), Ulsan 44919, Republic of Korea*
[3] *Institute of Nanobio Convergence Technology, Lemonex Inc., Seoul 08826, Republic of Korea*
[4] *College of Pharmacy, Ajou University, Worldcuplo 206, Yeongtong-gu, Suwon 16499, Republic of Korea*
[5] *Department of Chemistry, Korea Advanced Institute of Science and Technology (KAIST), Daejeon 34141, Republic of Korea*
[§] *These authors contributed equally to this work.*

Received: 25 July 2016
Revised: 26 September 2016
Accepted: 4 October 2016

© Tsinghua University Press and Springer-Verlag Berlin Heidelberg 2016

KEYWORDS
bioimaging,
carbon dot,
gene delivery,
RNA interference,
targeted cancer therapy

ABSTRACT

Small interfering RNA (siRNA) is an attractive therapeutic candidate for sequence-specific gene silencing to treat incurable diseases using small molecule drugs. However, its efficient intracellular delivery has remained a challenge. Here, we have developed a highly biocompatible fluorescent carbon dot (CD), and demonstrate a functional siRNA delivery system that induces efficient gene knockdown *in vitro* and *in vivo*. We found that CD nanoparticles (NPs) enhance the cellular uptake of siRNA, via endocytosis in tumor cells, with low cytotoxicity and unexpected immune responses. Real-time study of fluorescence imaging in live cells shows that CD NPs favorably localize in cytoplasm and successfully release siRNA within 12 h. Moreover, we demonstrate that CD NP-mediated siRNA delivery significantly silences green fluorescence protein (GFP) expression and inhibits tumor growth in a breast cancer cell xenograft mouse model of tumor-specific therapy. We have developed a multifunctional siRNA delivery vehicle enabling simultaneous bioimaging and efficient downregulation of gene expression, that shows excellent potential for gene therapy.

1 Introduction

RNA interference (RNAi) is a biological process discovered by A. Fire and C. C. Mello in 1998, where mRNA is sequence-specifically cleaved and degraded by small interfering RNA (siRNA), resulting in target gene silencing [1–3]. The RNAi pathway is accomplished by cellular machinery that requires the RNA-

Address correspondence to Dal-Hee Min, dalheemin@snu.ac.kr; Byeong-Su Kim, bskim19@unist.ac.kr; Younghoon Lee, younghoon.lee@kaist.ac.kr

induced silencing complex (RISC) for target RNA degradation [4–7]. Due to the convenience of transient target gene knockdown using short RNAs whose sequences can be designed based on a target mRNA sequence, RNAi has been widely used for both basic biological research and biomedical applications [8]. For therapeutic applications, siRNAs can be readily designed to silence target genes responsible for certain diseases, suggesting huge potential as a way of treating traditionally untargetable diseases [9, 10]. However, their gene silencing efficacy for disease treatment is limited by nuclease-mediated siRNA degradation and low intracellular uptake of siRNA; therefore, an efficient siRNA delivery system is urgently needed [11, 12].

To develop a therapeutic siRNA delivery system, various nanoparticles (NPs) including gold, magnetic, quantum dot, and silica NPs were employed in addition to cationic polymers and liposomes [13–22]. In general, cationic polymers have shown relatively high cytotoxicity [23]. Many NP-based siRNA delivery systems require chemically modified siRNAs and/or conjugation of siRNAs onto NP surfaces with subsequent purification of the siRNA conjugated NPs [9, 10]. These approaches possess limitations including time-consuming, multi-step processes, high costs, and labor-intensiveness. Therefore, development of a biocompatible, efficient, easy-to-prepare siRNA delivery system is an urgent issue for practical and clinical applications of siRNA-mediated gene silencing.

Recently, carbon NPs (also known as carbon dots, CDs), a new class of carbon-based nanomaterial, has received significant attention due to its low cytotoxicity, simple preparation, high chemical stability, and unique optical properties, similar to semiconducting quantum dots [24–31]. On top of the intense fluorescence of CDs, their surface functional groups enhance aqueous solubility and provide flexibility of chemical modifications of the surface, such as conjugation of targeting ligands. Taking advantage of their excellent optical and chemical properties, CDs have been employed in a number of biological applications, including plasmid DNA/drug delivery, bioimaging, biosensing, and photo-induced therapy [32–40]. Although CD derivatives provide good potential for therapeutic applications, a challenge still remains for an *in vivo* therapeutic system that requires targeting capability and biological imaging ability to enhance tumor-specific treatment following systemic administration.

We synthesized highly fluorescent poly(ethyleneimine) (PEI)-passivated CDs (CD-PEI) as a novel carrier for siRNA delivery to simultaneously achieve bioimaging and target gene knockdown. CD-PEI was synthesized via one-step household microwave pyrolysis using citric acid and PEI. In this synthetic scheme, the PEI used as a passivation agent plays multiple roles—enhancing fluorescence of CD, siRNA loading capacity, and cellular uptake [41]. Prior to cellular treatment, the siRNA/CD-PEI complex was first prepared through electrostatic interaction between siRNA and CD-PEI by simply mixing the two components in buffered solutions. We showed that the siRNAs complexed with CD-PEI were protected from ribonuclease (RNase)-mediated degradation, implying longer chemical stability compared to naked siRNA *in vivo*. The siRNA/CD-PEI complex was successfully employed for the sequence-specific knockdown of target gene expression *in vitro* and *in vivo*, as well as for convenient monitoring of the cellular uptake of the therapeutic complex in real time after systemic introduction (Fig. 1).

2 Experimental

2.1 Materials

Citric acid and branched PEI (M_W = 10,000) were purchased from Sigma-Aldrich and Polysciences, Inc., respectively. Phosphate buffered saline (PBS, 10×), Dulbecco's modified Eagle's medium (DMEM), and fetal bovine serum (FBS) were purchased from WELGENE, Korea. SYBR® Gold nucleic acid gel stain was purchased from Life Technologies, USA. Cell counting kit-8 (CCK-8) was purchased from Dojindo Laboratories (Japan). RNase was purchased from New England Biolabs, USA. All siRNA was purchased from Bioneer, Republic of Korea.

2.2 Synthesis of CD-PEI

To synthesize CD-PEI, 250 mg of PEI (25 mmol) was first dissolved in 5 mL water, and 500 mg of citric acid (2.6 mmol) was added. The transparent mixed

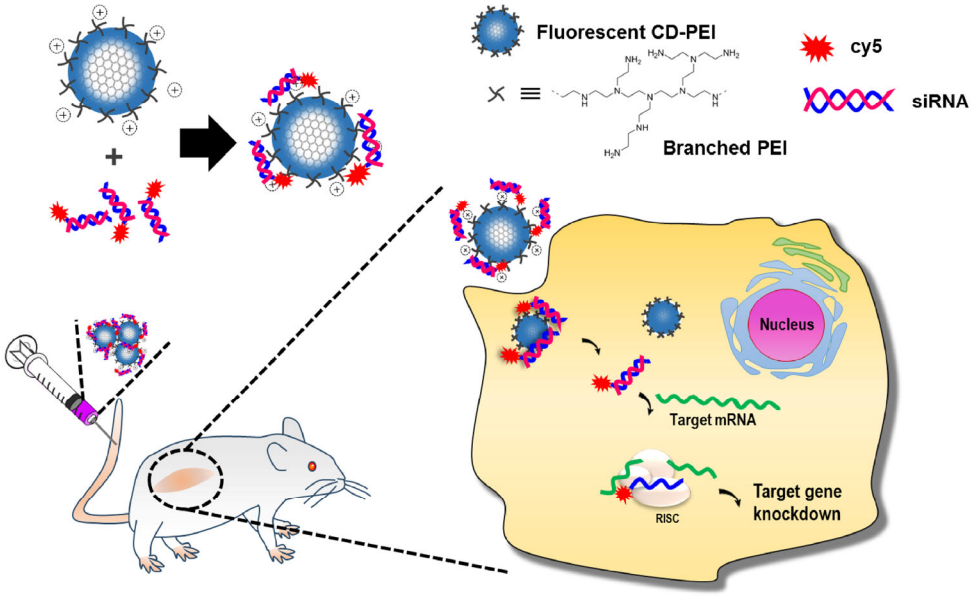

Figure 1 Strategy for CD-PEI-mediated siRNA delivery and bioimaging. The CD-PEI and siRNA complex is formed by electrostatic interaction between CD-PEI and siRNA. After cellular uptake of the siRNA/CD-PEI complex, siRNA is released from CD-PEI and target gene knockdown is achieved by an siRNA-RISC complex. The intrinsic fluorescence of CD-PEI enabled fluorescent image-based monitoring of cellular uptake of the siRNA/CD-PEI complex and intracellular localization of CD-PEI in living cells.

solution was placed into a microwave oven and heated for 2 min. After the solution cooled down to room temperature, the obtained white-yellow solid was dissolved in 5 mL of water and dialyzed using SpectraPore (M_W = 12,000) for 2 days to remove excess salts, unreacted citric acid and free PEI.

2.3 Characterizations

A UV/vis spectrophotometer (UV-1800, Shimadzu, Japan) was used to measure the absorbance of the CD-PEI derivatives solution. Fluorescence data was obtained using a fluorometer (Agilent, USA). Three-dimensional fluorescence spectra of CD-PEI derivatives were obtained with a spectrofluorometer FP-8300 (JASCO, USA). Transmission electron microscopy (TEM; JEM-2100, JEOL, Japan) and atomic force microscopy (AFM; Dimension 3100, Veeco, USA) were performed to observe the size and morphology of CD-PEI. X-ray diffraction (XRD) measurements were carried out with a high-power X-ray diffractometer (Rigaku Co., D/MAZX 2500V/PC, Japan) from 10° to 50°. X-ray photoelectron spectroscopy (XPS) (K-alpha, Thermo Fisher, USA) and FT-IR (Agilent, USA) were used for the characterization of functional groups. An element analyzer (Thermo Scientific, USA) was used to obtain weight percentages of carbon, hydrogen, nitrogen, and oxygen components of CD-PEI.

2.4 Photoluminescence lifetime measurement

The exciton lifetime was determined using the time-correlated single photon counting (TCSPC) technique. A computer-controlled diode laser with 375 nm wavelength, 54 ps pulse width, and 40 MHz repetition rate was used as an excitation source. The photoluminescence (PL) emission was spectrally resolved using collection optics and a monochromator (PicoQuant, Germany). The TCSPC module (PicoHarp 300E, PicoQuant, Germany) with an MCP-PMT (R3809U-5x series, Hamamatsu, Japan) was used for ultrafast detection. The total instrument response function (IRF) for PL decay was less than 30 ps, and the temporal time resolution was less than 10 ps. The deconvolution of actual fluorescence decay and IRF was performed using fitting software (FluoFit, PicoQuant, Germany) to deduce the time constant associated with each exponential decay.

2.5 Measurement of quantum yield (QY)

The QY is calculated using the slope of the line

determined from the plot of the absorbance against the integrated fluorescence intensity as a comparative method. The QY (Q) can be calculated using the following equation

$$Q = Q_R ((m/m_R)(n^2/n_R^2))$$

where m is the slope of the line obtained from the plot of the integrated fluorescence intensity versus absorbance, n is the refractive index of the solvent, and the subscript R refers to the reference fluorophore of known quantum yield.

2.6 Loading capacity test and heparin polyanion competition assay

Polyacrylamide gel electrophoresis (PAGE) analysis was used to measure the loading capacity, and heparin polyanion competition assay of siRNA/CD-PEI complexes was performed. The siRNAs at various concentrations (20–150 pmol) were incubated with 1 μg of CD-PEI in 20 μL PBS. After 1 h incubation, the gel was stained with SYBR gold staining reagent. For the heparin polyanion competition assay, heparin (0–50 μg) was added to the siRNA/CD-PEI mixtures prior to gel electrophoresis to induce release of siRNA from CD-PEI.

2.7 RNase protection assay

PAGE analysis was carried out to estimate the protection of the siRNA against RNase-mediated degradation in the presence of CD-PEI complexes. RNase (25 μg) was first incubated with siRNA and siRNA/CD-PEI complexes in 20 μL PBS for 1 h before gel electrophoresis and SYBR gold staining were performed.

2.8 Loading capacity test and heparin polyanion competition assay

We cultured HeLa cells constitutively expressing GFP (GFP-HeLa) and MDA-MB-231 cells (1×10^4 cells/well) in a 96-well plate for 24 h, followed by incubation with various concentrations of CD-PEI or PEI in serum-containing media. After 12 h incubation, the cells were carefully washed with 1× PBS and then CCK-8 assay solution and serum-free media were added and incubated for 1 h. Absorbance at 450 and 670 nm was then measured using a microplate reader (Molecular Devices, Inc., USA).

2.9 Cellular uptake study

The siRNA/CD-PEI complex, prepared using Cy5-conjugated siRNA targeting GFP (Cy5-siGFP) and vascular endothelial growth factor (VEGF) gene expression using an siRNA sequence designed to target VEGF (siVEGF) (50 nM), was combined with GFP-HeLa and MDA-MB-231 cells in serum-free medium in a 4-well glass plate for 12 h (final volume, 500 μL). Cell medium was then replaced with serum-containing fresh medium and cell images were obtained using a Ti inverted fluorescence microscope (Olympus, Japan) with a 20× objective lens.

For time-lapse fluorescence tracking of Cy5-siGFP and CD-PEI, GFP-HeLa cells were incubated with Cy5-siGFP/CD-PEI complexes in serum-free medium for 12 h in a 96-well plate (μClear® microplate, Greiner, Austria; final volume, 50 μL). The fluorescent signal in the cells was observed, after changing to serum-containing fresh medium, using a DeltaVision Elite imaging system and an IN Cell Analyzer2000 (GE Healthcare, USA) at various time points.

2.10 Flow cytometry

GFP-HeLa cells were treated with siGFP/CD-PEI complex in serum-free medium for 12 h (final volume, 500 μL, [siRNA] = 50 nM). Cell medium was then changed to serum-containing fresh medium and incubated for 2 h. After washing with 1× PBS, the cells were collected after treatment with trypsin-EDTA for 3 min and then 10% FBS was added to the collected cells, followed by centrifugation (1,200 rpm, 3 min). The cells were finally washed with 1× PBS and their fluorescence was measured by flow cytofluorometry (FACS Canto, Becton Dickinson, USA).

2.11 Semi-quantitative RT-PCR

MDA-MB-231 cells were seeded in a 12-well plate (1.2×10^5 cells/well). After 24 h incubation, the cells at 70%–80% confluency were treated with siVEGF and lipofectamine (Lipo) for 4 h, and siVEGF with PEI and with CD-PEI for 12 h in serum-free medium (final volume; 500 μL). The cells were then further incubated

up to 48 h with serum-containing fresh medium prior to functional evaluation.

To assess the immunostimulatory activities, CD-PEI and siRNA/CD-PEI were cultured with GFP-HeLa cells for 12 h, followed by washing and addition of fresh medium. To boost the immune response as a control, poly I:C (P/C) was incubated for 6 h with Lipo.

For the semi-quantitative RT-PCR, total RNA was collected using Trizol reagent (Invitrogen, USA) and analyzed to measure the quantity and quality of the extracted RNA based on absorbance at 260 nm (A_{260}) and RNA/protein ratio (A_{260}/A_{280}) by using a UV-Vis spectrophotometer (Nanodrop Take3 or fluorometer (BioTek, USA)). cDNA was then synthesized from 800 ng of total RNA from MDA-MB-231 cells for VEGF gene downregulation and 700 ng of total RNA from GFP-HeLa cells for immune response analysis by reverse transcription using Superscript II reverse transcriptase (Invitrogen, USA) based on the manufacturer's protocol. Amplification was then performed using a thermal cycler (BioRad, USA) and the following primer pairs:

(1) VEGF forward primer: 5′-AGG AGG GCA GAA TCA TCA CG -3′

(2) VEGF reverse primer: 5′-CAA GGC CCA CAG GGA TTT TCT-3′

(3) GAPDH forward primer: 5′-TTG TTG CCA TCA ATG ACC CCT TCA TTG ACC-3′

(4) GAPDH reverse primer: 5′-CTT CCC GTT CTC AGC CTT GAC GGT G-3′

(5) TLR3 forward primer: 5′-AGC CAC CTG AAG TTG ACT CAG G-3′

(6) TLR3 reverse primer: 5′-CAG TCA AAT TCG TGC AGA AGG C-3′

(7) INF-β forward primer: 5′-ACC AAC AAG TGT CTC CTC CA-3′

(8) INF-β reverse primer: 5′-GAG GTA ACC TGT AAG TCT GT-3′

(9) β-actin forward primer: 5′-GCT CGT CGT CGA CAA CGG CTC-3′

(10) β-actin reverse primer: 5′-CAA ACA TGA TCT GGG TCA TCT TCT-3′

The following PCR reaction conditions were used. VEGF: 2 min at 94 ℃, (20 s at 94 ℃, 30 s at 60 ℃, 30 s at 72 ℃) × 30 cycles; GAPDH (used as a housekeeping gene): 5 min at 94 ℃, (30 s at 94 ℃, 30 s at 60 ℃, 30 s at 72 ℃) × 26 cycles; Toll-like receptor 3 (TLR3) and INF-β: 5 min at 94 ℃, (30 s at 94 ℃, 30 s at 55 ℃, 45 s at 72 ℃) × 30 cycles; β-actin: 5 min at 94 ℃, (30 s at 94 ℃, 30 s at 58 ℃, 30 s at 72 ℃) × 35 cycles. The PCR products were analyzed by 1.2% TAE (Tris-acetate-EDTA) agarose gel retardation assay and the bands were confirmed using a Gel Doc imaging system (ATTO, Republic of Korea). Relative band intensities were quantified using Image J software, and VEGF gene expression level was normalized relative to GAPDH expression level.

2.12 *In vivo* study

All animal experiments were carried out in compliance with the Institutional Animal Care and Use Committees (IACUC) of Seoul National University. Balb/c male nude mice (5-weeks old) were purchased from ORIENT (Republic of Korea). Tumor-bearing xenograft mice were prepared by subcutaneous injection of GFP-HeLa cells (2×10^5 cells in 100 μL of 1× PBS) to Balb/c male nude mice (6-weeks old). To monitor the fluorescence changes within tumors, we prepared siGFP (1 nmol) with PEI and CD-PEI, and 1× PBS as a control in a final volume of 100 μL; suspensions were injected once every other day directly into tumors after tumor volume reached ~70 mm^3, n = 3. GFP and Cy5 fluorescence signals were monitored at designated time points (0, 2, and 4 days) using an Optix MX3 optical molecular imaging system (GE Healthcare Life Sciences, USA) at 490 and 650 nm excitation wavelengths, respectively. The tumors were excised from the sacrificed mice and GFP and Cy5 fluorescence were again visualized using the optical molecular imaging system. To monitor the biodistribution of particles, FITC-labelled CD-PEI in a total volume of 100 μL was administered to tumor-bearing xenograft mice by intravenous (IV) injection (n = 3). The green fluorescence from the CD-PEI throughout the body, and that from excised organs and tumors, was obtained after injection at 24 h using the Optix MX3 optical molecular imaging system at 490 nm excitation wavelength. To investigate anti-tumor efficacy, we prepared siVEGF (1 nmol) with PEI and CD-PEI, and 1× PBS as a control in a final volume of 50 μL, then injected the suspensions intravenously at 0, 5, and

10 days after the tumor volume of MDA-MB-231 implanted xenograft mice reached ~60 mm^3, n = 4. The changes in tumor volume and body weight were monitored in each group over 14 days. The tumor volumes were calculated by using the following equation

$$\text{Tumor volume} = \text{Length} \times (\text{width})^2 \times {}^1/_2$$

where the length and width are the longest and shortest diameters (mm) of the tumor, respectively. The tumor volumes were calculated relative to the initial volumes.

2.13 Statistical analysis

P-values, referring to statistical significance of at least three independent experiments, were determined based on the Student's *t*-test using GraphPad Software.

3 Results and discussion

3.1 Synthesis & characterization of CD-PEI

CD-PEI was synthesized by dehydrating citric acid and PEI using the microwave-assisted pyrolysis method. The UV–Vis spectrum of CD-PEI in Fig. 2(a) shows two UV/Vis absorption peaks at 243 and 354 nm wavelengths, corresponding to the typical absorption of an aromatic moiety having an sp^2 carbon network and the $n \rightarrow \pi^*$ transition of carbonyl groups, respectively [42]. CD-PEI displayed a bright blue color under UV irradiation (λ_{ex} = 360 nm) with an emission maximum at 450 nm (inset in Fig. 2(a)). The fluorescence emission spectra of CD-PEI showed an excitation wavelength dependency, similar to the previously reported CDs (Fig. 2(b) and Fig. S1(a) in the Electronic Supplementary Materials (ESM)). The QY of CD-PEI was measured as 18.8% using quinine sulfate as a reference. The relatively high QY of CD-PEI might be due to surface passivation by PEI which could reduce the non-radiative recombination of localized electron–hole pairs through nucleophilic reaction between alkylamines of PEI and carboxylic/epoxy groups of CDs [43]. The exciton lifetime of CD-PEI was determined as 5.51 ns by TCSPC (Fig. S1(b) in the ESM). The CD-PEI was highly stable in aqueous solution with a zeta-potential of +21.7 (± 0.43) mV at pH 7.4. The amount of conjugated PEI in CD-PEI was determined by measuring the UV/Vis absorbance of the cuprammonium complex of CD-PEI at 630 nm, which yielded 29.8 wt.% of PEI in CD-PEI [44].

FT-IR spectroscopy was then performed to characterize the functional groups on CD-PEI. The CD-PEI showed a broad peak at 3,394 cm^{-1} corresponding to O–H and N–H groups and peaks related to amide bonds at 1,700 cm^{-1} (C=O stretching), 1,576 cm^{-1} (N–H in-plane), and 1,389 cm^{-1} (C–N stretching) (Fig. 2(c)). XPS revealed that CD-PEI contained carbon (C 1s, 284 eV), nitrogen (N 1s, 400 eV), and oxygen (O 1s, 532 eV). Deconvoluted high-resolution XPS spectra of CD-PEI (C 1s) showed peaks corresponding to C=C (284.1 eV), C–O (285.9 eV), C–N (286.9 eV), C=O (288.6 eV), and COOH (290.1 eV) bonds (Fig. 2(d)). Elemental analysis revealed the composition of CD-PEI as C 49.73%, H 7.56%, N 11.37%, and O 31.26%. TEM showed the diameter of CD-PEI ranging from 3 to 7 nm, with an average diameter of 5.1 ± 1.2 nm. The interlayer spacing of 0.21 nm agreed well with the spacing of (100) facet graphite (Fig. 2(e) and Fig. S1(c) in the ESM) [45]. The AFM line scans showed 5.8 nm for the topographic height of CD-PEI that matched well with the observations from TEM analysis (Fig. 2(f)). The XRD pattern of CD-PEI in Fig. S1(d) in the ESM displayed a broad peak centered at 0.42 nm.

3.2 Formation of siRNA/CD-PEI complexes

Prior to evaluation of gene knockdown efficiency, we measured the siRNA loading capacity of CD-PEI. We first allowed the siRNA/CD-PEI complexes to form by mixing CD-PEI and siRNA at various concentrations in 1× PBS (pH 7.4) for 30 min at room temperature, and assessed the formation of siRNA/CD-PEI complexes by PAGE. As described above, siRNA/CD-PEI complexes were formed by electrostatic interaction between the positive charges on the surface of PEI-passivated CD and the negative charges on the phosphate backbone of siRNA. The assembled siRNA/CD-PEI complex was not expected to migrate towards positive electrode in PAGE due to the increased size and reduced negative charge. The siRNA loading capacity of CD-PEI was estimated and 1 μg of CD-PEI was found to be sufficient for loading of 100 pmol of

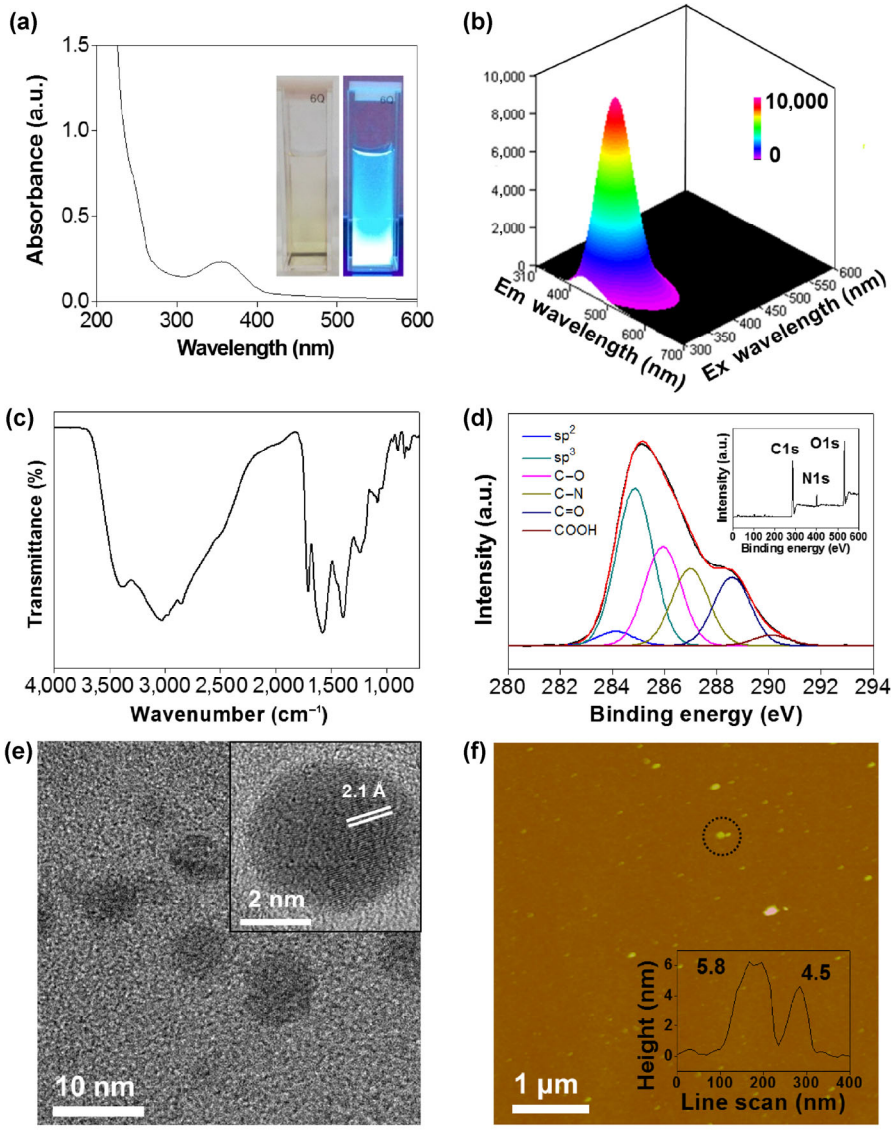

Figure 2 Characterization of CD-PEI. (a) UV–vis absorption spectrum of CD-PEI. Inset shows a photo of the CD-PEI suspension (left) under ambient room light and (right) UV illumination at 360 nm. (b) Three-dimensional fluorescence spectra of CD-PEI under varying excitation wavelengths from 300 to 800 nm with 10 nm increments. (c) FT-IR spectrum of CD-PEI. (d) Deconvoluted high-resolution XPS C 1s peak of CD-PEI with the survey XPS spectra of CD-PEI in the inset. (e) TEM image of CD-PEI. Inset shows a representative image of single CD-PEI with lattice spacing of 0.21 nm. (f) An AFM topography image of CD-PEI obtained under constant height contact scanning mode is shown with a line scan profile in the inset.

siRNA and 50 pmol of Cy5-siRNA (Cy5 dye-labelled siRNA) according to PAGE analysis (Fig. 3(a) and Fig. S2(a) in the ESM).

Next, zeta-potential was measured to estimate the surface charge of the complex because this could affect the cellular uptake process and transfection efficiency [33]. After complexation of 1 μg CD-PEI with 50 pmol siRNA and 50 pmol Cy5-siRNA, the zeta-potential of CD-PEI changed from +21.7 (± 0.4) to +3.4 (± 0.7) and +5.3 (± 0.4) mV, respectively at pH 7.4. The decrease in zeta-potential after siRNA addition to CD-PEI suggested the successful complexation of siRNA to CD-PEI and the resulting positive zeta-potential of the siRNA/CD-PEI complex implied the possibility of favorable interaction with the negatively charged cell surface to promote its cellular uptake. Dynamic light scattering (DLS) analysis also showed the increase of size distribution after complexation in buffered

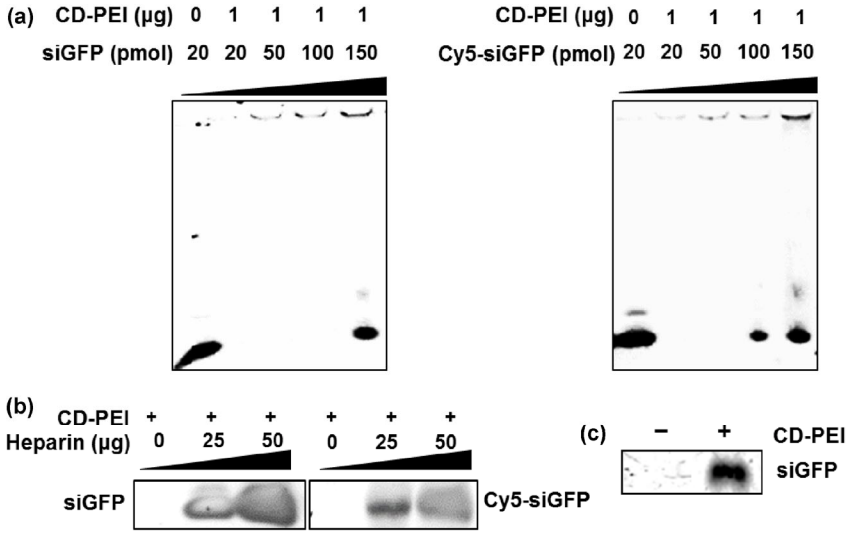

Figure 3 PAGE analysis to investigate siRNA loading of CD-PEI. (a) Mixed solutions of CD-PEI with siGFP and Cy5-siGFP at various concentrations were prepared and loaded for PAGE. Gel images suggested that maximum siRNA loading could be achieved using ~150 and ~100 pmol of siGFP and Cy5-siGFP, respectively, with 1 μg of CD-PEI. (b) PAGE analysis was performed after heparin was added to mixtures of CD-PEI/siRNA. The polyanion competition assay revealed that the siRNA loaded onto CD-PEI could be released from CD-PEI upon treatment with polyanionic heparin. (c) Gel image showing that RNase-mediated siRNA degradation was inhibited in the presence of CD-PEI. In contrast, free siRNA without CD-PEI was completely degraded upon addition of RNase.

conditions (Fig. S2(c) in the ESM). Taken together, zeta-potential, PAGE analysis, and DLS data suggested the successful formation of the siRNA/CD-PEI complex.

3.3 siRNA release and protection against RNase-mediated degradation *in vitro*

To achieve successful siRNA delivery and efficient target gene knockdown, siRNA should be released from the CD-PEI in cell cytoplasm to induce RNAi and degrade target mRNA. Heparin has been utilized in medicine as an anticoagulant as well as a reagent to release anionic oligonucleotide from cationic NPs functioning as a polyanionic polymer *in vitro* [18]. Therefore, we performed the heparin competition assay to investigate the release of siRNA from CD-PEI upon addition of heparin. Figure 3(b) shows that band intensities corresponding to the released siRNA increased dose-dependently with treatment of heparin up to 50 μg, whereas the band was not observed in the absence of heparin, suggesting conditional release of siRNA from CD-PEI.

We next performed the *in vitro* RNase protection assay to investigate whether siRNA in the siRNA/CD-PEI complex maintains its chemical structure in the presence of RNase under physiological conditions. For efficient gene silencing, it is necessary to maintain the chemical stability of siRNA in the siRNA/CD-PEI complex within biological environments until the complex reaches its target site [6]. Aqueous solutions of free siRNA and siRNA/CD-PEI complexes were prepared and incubated with RNase (25 μg) in 20 μL PBS solution for 1 h at 37 °C. PAGE analysis was then performed after post-incubation with heparin (50 μg) for 10 min. As shown in Fig. 3(c) and Fig. S2(b) in the ESM, an intense siRNA band was observed even after treatment with RNase, suggesting protection of siRNA from RNase mediated-degradation in the presence of CD-PEI. In contrast, free siRNA was completely degraded by RNase under the same experimental conditions. The complexation between siRNA and PEI on the CD surface provided protection for siRNA against nuclease degradation, which might prevent interaction between RNase and siRNA/CD-PEI complexes through steric hindrance effects and low electrostatic interaction. This result was in agreement with previous studies of PEI-passivated or complexed NPs [46] and indicates that CD-PEI may serve as an efficient siRNA delivery carrier because it effectively

condenses with siRNA and protects the adsorbed siRNA from enzymatic cleavage mediated by RNase.

3.4 Cytotoxicity of CD-PEI in HeLa and MDA-MB-231 cells

To be a practically useful siRNA delivery vehicle, low cytotoxicity is an essential prerequisite. Therefore, we measured the viability of mammalian cells, HeLa and MDA-MB-231, after treatment with CD-PEI at various concentrations for 12 h using a CCK-8 cell viability assay 8 kit. It is well known that PEI exhibits cytotoxicity induced by cell membrane damage due to the highly positive charges of PEI. Therefore, wider applications of PEI itself in gene delivery have been restricted, especially in *in vivo* biomedical applications [47, 48]. In contrast to PEI itself, CD-PEI showed notably lower cytotoxicity (Fig. S3 in the ESM). More than 90% of cells were viable at all concentrations of CD-PEI tested. We used a maximum concentration of CD-PEI of 50 $\mu g \cdot mL^{-1}$ throughout the present study, ensuring more than 90% cell viability. We assume that CD-PEI reduces the toxicity of PEI because the density of amine groups presenting positive charges on PEI decreased during the passivation process of CD while maintaining its net positive charge [49, 50]. In addition, the reduced degree of freedom of flexible PEI polymer in CD-PEI may decrease the number of positively charged functional groups of PEI that can interact with the cell surface, resulting in lower cytotoxicity.

3.5 Intracellular uptake and bioimaging in living cells

In accordance with previous research confirming endocytosis of PEI NPs and PEI-complexed NPs, the fluorescent CD-PEI was expected to enable cellular imaging of the endocytosed siRNA/CD-PEI complex in cytoplasm, and monitoring of the dissociation of the siRNA from the delivery vehicle if dye-labelled siRNA was employed. After we confirmed that the major optical characteristics of CD-PEI remained unaffected after formation of Cy5-siRNA/CD-PEI (Fig. S4 in the ESM) and that the intracellular localization of Cy5-siRNA was untraceable when administered alone to cells, we investigated the cellular uptake and intracellular localization of the siRNA/CD-PEI complexes inside cell cytoplasm. We used Cy5-siGFP and GFP-HeLa. After treatment with siGFP/CD-PEI complex in GFP-HeLa cells for 12 h, the Cy5-siGFP/CD-PEI complex was visualized in GFP-HeLa cells by monitoring the blue and red fluorescence originating from CD-PEI ($\lambda_{ex}/\lambda_{em}$ = 370/443 nm) and Cy5-siGFP ($\lambda_{ex}/\lambda_{em}$ = 650/670 nm), respectively. Cell images in Fig. 4(a) and Fig. S5 in the ESM show fluorescence corresponding to Cy5-siGFP (red) and CD-PEI (blue) in the cytoplasm. We observed that the inherent green fluorescence ($\lambda_{ex}/\lambda_{em}$ = 495/521 nm) from GFP-HeLa cells significantly decreased, indicating that GFP expression was downregulated by siGFP targeting of GFP mRNA. Bio-TEM images of the GFP-HeLa cells treated with siGFP/CD-PEI also exhibited the endocytosed CD-PEI around the perinuclear region in cell cytoplasm with a small increase in size (Fig. 4(b)) [51, 52]. It is well known that the aggregation of PEI-complexed NPs and PEI-oligonucleotide was reduced under low pH conditions due to electrostatic repulsive interactions between the complexes [53, 54]. In the present study, CD-PEI exhibited a smaller overall size at low pH (Fig. S6 in the ESM). Even though the size of the complex seemed to be slightly increased in pH 7.0 buffered solution by aggregation, we think that the proton-sponge effect accelerated the stable dispersion through decreased aggregation at pH 5.0 in buffered solution (Fig. S6 in the ESM).

To more precisely investigate the release kinetics of siRNA from CD-PEI complexes corresponding to the time-dependent distribution of the CD-PEI and Cy5-siGFP inside cell cytoplasm, the fluorescence signals were observed in living cells at various time points after Cy5-siGFP/CD-PEI complex treatment (Figs. 4(c) and 4(d), and Fig. S7 in the ESM). After 2 h incubation, pinkish purple fluorescence was observed in cell cytoplasm, derived from merging of the blue and red fluorescence, indicating that the Cy5-siGFP/CD-PEI complex remained intact without notable siRNA release after cellular uptake at this early time point. However, during further incubation, blue and red fluorescence signals were separated from each other in the cytoplasm, suggesting the release of Cy5-siGFP from CD-PEI in cell cytoplasm over time. [55] Taken

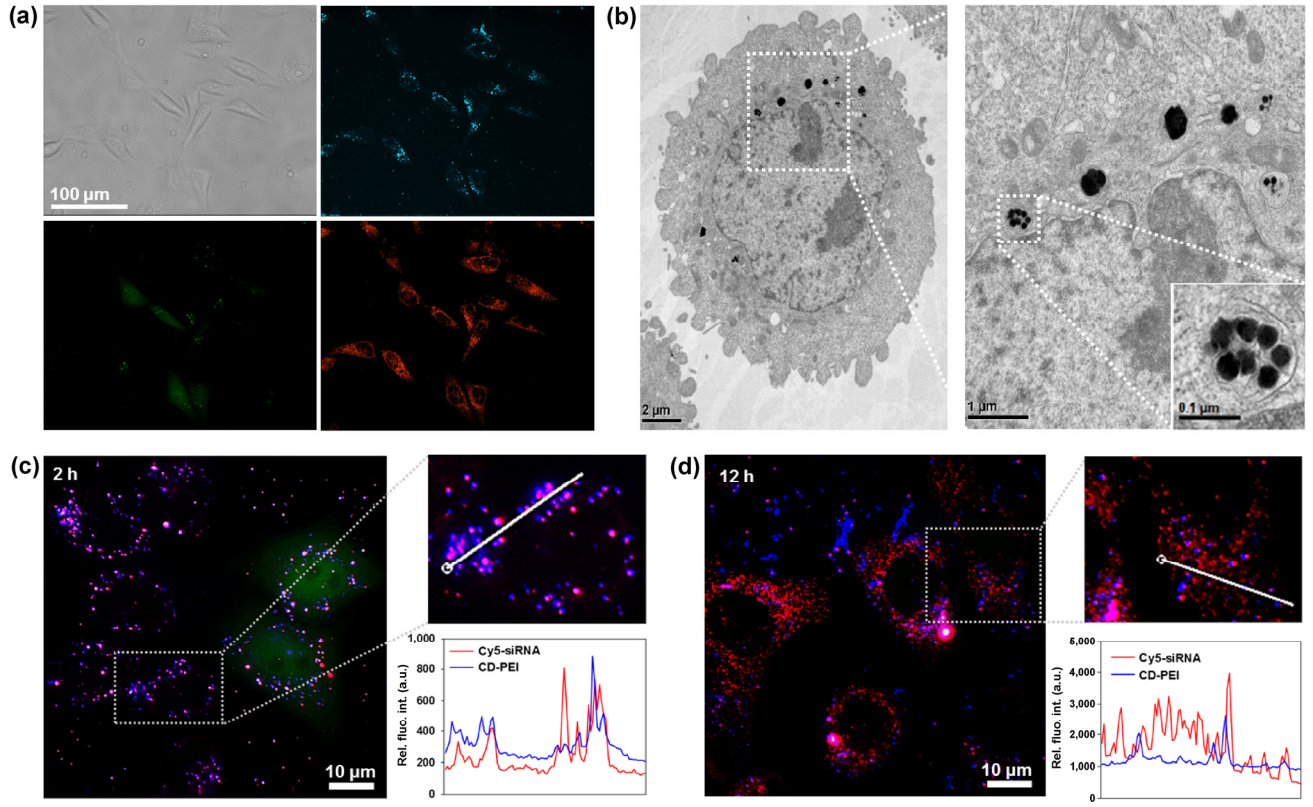

Figure 4 Cellular internalization *in vitro*. (a) Fluorescent images of GFP-HeLa cells treated with Cy5-siGFP/CD-PEI (blue, CD-PEI; green, GFP; red, Cy5-siGFP). (b) Bio-TEM images of GFP-HeLa cells treated with CD-PEI showing the presence of the internalized CD-PEI in cytoplasm. (c) and (d) Fluorescence signals from Cy5-siGFP (red) and CD-PEI (blue) in the cytoplasm of GFP-HeLa cells treated with Cy5-siGFP/CD-PEI. Relative fluorescence intensities of CD-PEI and Cy5-siGFP were measured along with line scan profile in living cells. After 12 h incubation of the GFP-HeLa cells treated with siGFP/CD-PEI, fluorescence corresponding to Cy5-siGFP was hardly co-localized with blue fluorescence corresponding to CD-PEI (d) whereas Cy5-siGFP fluorescence mostly overlapped with CD-PEI fluorescence at 2 h post-incubation (c), implying that Cy5-siGFP become released from its delivery carrier, CD-PEI, over time in cytoplasm.

together, the time dependent bioimaging based on the highly fluorescent CD was successfully demonstrated in live cells without notable cytotoxicity.

3.6 RNAi based on CD-PEI against target gene *in vitro*

Next, we quantitatively evaluated the knockdown of GFP expression induced by siGFP/CDPEI in GFP-HeLa cells. GFP-expressing HeLa cells were first treated with 50 nM of siGFP/CD-PEI in a 12-well plate for 12 h. Lipo and PEI were used as controls. At 48 h post-transfection, cell medium was removed and replaced with fresh serum-containing medium. Then, relative GFP expression levels were estimated by observing fluorescent images of the cells using a fluorescence microscope and flow cytometry. Images in Fig. 5(a) and Fig. S8 in the ESM show a notable decrease in green fluorescence in GFP-HeLa cells treated with siGFP/Lipo and siGFP/CD-PEI compared to the HeLa cells treated with PEI, Lipo, or CD-PEI only. Figure 5(b) shows flow cytometry histograms of cell populations versus green fluorescence intensity. To more precisely analyze the data, we divided the histograms into two regions, M1 and M2, respectively indicating low and high green fluorescence intensities of GFP compared to untreated cells (control), and mean fluorescence in each region was calculated and presented in a bar-graph in Fig. 5(c). It is notable that the cells treated with siGFP/CD-PEI showed the most significant decrease in mean GFP fluorescence both in M1 and M2. Overall mean fluorescence of GFP based on both M1 and M2 also supported the most efficient GFP

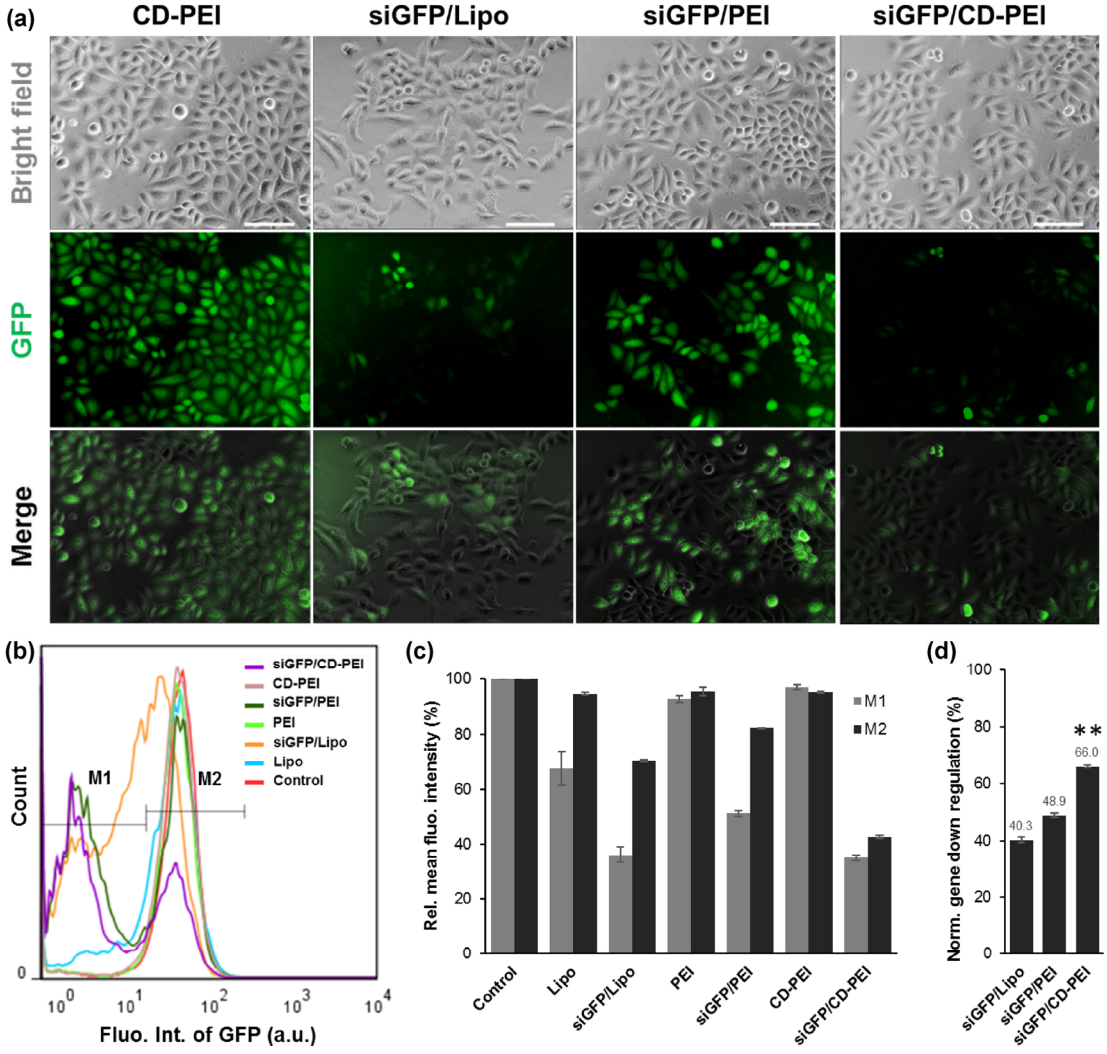

Figure 5 Downregulation of GFP gene expression using siGFP/CD-PEI complexes. (a) Fluorescence microscope images of GFP-HeLa cells treated with siGFP/CD-PEI were obtained at 12 h post-incubation. (b) Mean fluorescence of GFP expression in the GFP-HeLa cells was quantitatively measured by flow cytometry. M1 and M2 indicate two populations of cells expressing GFP to different degrees due to significant suppression of GFP expression (M1) and little or no downregulation of GFP expression (M2). (c) Relative GFP fluorescence level and (d) relative GFP gene downregulation observed from the flow cytometry measurements in (b) are presented in bar graphs. Scale bar is 100 μm. *P*-values were calculated by Student's *t*-test: ** for $P < 0.01$, $n = 3$.

knockdown in the cells treated with siGFP/CD-PEI (Fig. 5(d)). The mean green fluorescence significantly decreased in the cells treated with siGFP/CD-PEI down to 34.0% relative to the untreated control, compared to those with siGFP/Lipo (59.7%) and siGFP/PEI (51.1%). It is notable that CD-PEI-mediated siGFP delivery showed better gene silencing than Lipo as well as higher cell viability (92.3%) compared to Lipo (77.3%) and PEI (75.3%) (data not shown). Lipo and PEI are well known as popular non-viral gene transfection agents but they exhibit high cytotoxicity at effective concentrations and/or during long time treatment. Collectively, the data suggest that CD-PEI is a more efficient siRNA delivery vehicle with lower cytotoxicity than Lipo or PEI.

Next, we investigated downregulation of siVEGF. VEGF plays a pivotal role in tumor growth, inducing angiogenesis by activation of endothelial cells through binding to the VEGF receptor and subsequent signal cascade [56, 57]. Therefore, the inhibition of VEGF expression has been one of the important goals of gene therapy strategies for treating various cancers. We

evaluated the knockdown of VEGF gene expression at mRNA level induced by siVEGF in complex with CD-PEI after monitoring the fluorescence from CD-PEI taken up into the cells (Fig. S9 in the ESM). MDA-MB-231 breast cancer cells were incubated with 50 nM siVEGF/CD-PEI complex for 12 h. At 48 h post-transfection, cell media was removed and replaced with fresh serum-containing media. Then, the VEGF gene expression level was estimated by semi-quantitative RT-PCR. Band intensities of VEGF gene in gel electrophoresis were normalized with respect to GAPDH. As shown in Fig. 6, RT-PCR results showed similarly efficient gene silencing of the VEGF gene by siVEGF/CD-PEI complexes down to 32.2% and by siVEGF/Lipo down to 32.9%. Under the same conditions in the absence of siVEGF, cell viability was slightly reduced to 94.6% after treatment with CD-PEI whereas the Lipo treatment induced a notable decrease in the cell viability down to 70.0%. Collectively, these data indicate that CD-PEI could be an efficient siRNA delivery carrier for siVEGF to silence therapeutically relevant VEGF gene expression in addition to siGFP for knockdown of a model gene, GFP. The CD-PEI-mediated siRNA delivery and knockdown of the target gene were successfully demonstrated in two different cancer cell lines—HeLa and MDA-MB-231.

3.7 Immune response study

With consideration for the possibility of unexpected immune responses to our gene delivery system, we investigated the immunostimulatory properties of CD-PEI and siRNA/CD-PEI complexes. It is reported that TLR3 recognizes double-stranded RNA (dsRNA) and induces type I interferon (IFN) by activating a variety of signal pathways, including production of cytokines and chemokines, and activation of NF-κB and MAP kinases [58–60]. Thus, investigating the masking ability of CD-PEI against potential immune response activated by siRNA introduction is important. We prepared GFP-HeLa cells treated with CD-PEI, siRNA/CD-PEI, and P/C as a control. The expression levels of TLR3 and IFN-β were measured by RT-PCR and gel electrophoresis. As shown in Fig. S10 in the ESM, induction of TLR3 and activation of INF-β were hardly observed in CD-PEI- and siRNA/CD-PEI-treated cells. Overall, the data suggest that CD-PEI can mask the immune responses activated by siRNA without showing immunostimulatory properties itself *in vitro*.

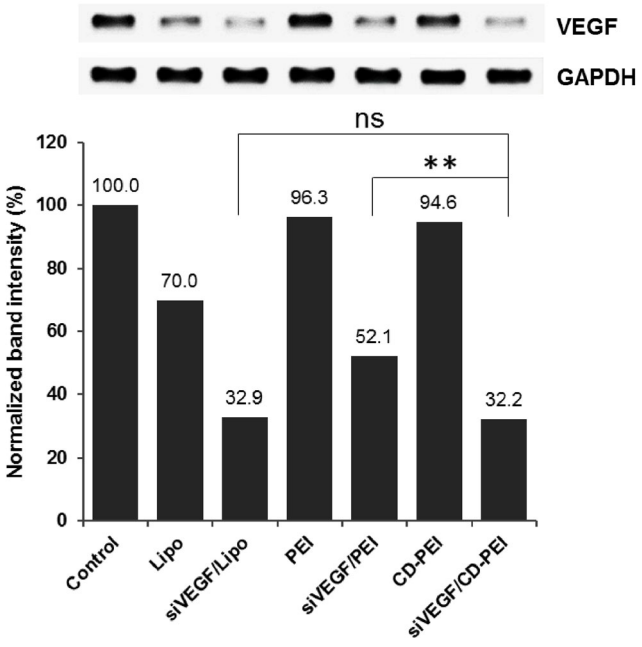

Figure 6 Expression level of VEGF and GAPDH in MDA-MB-231 cells. Gene expression levels were evaluated by semi-quantitative RT-PCR and gel electrophoresis. *P*-values were calculated by Student's *t*-test: ** for $P < 0.01$, $n = 3$.

3.8 Gene silencing in a xenograft mouse model

Encouraged by the successful demonstration in cultured cancer cells *in vitro*, we finally investigated the applicability of our CD-PEI-based siRNA delivery system in a mouse model. First, tumor-bearing xenograft mice were prepared by subcutaneous injection of GFP-HeLa cells, and then siGFP was introduced intratumorally, complexed with PEI or CD-PEI. Green fluorescence from GFP in tumors treated with siGFP/CD-PEI was significantly decreased compared to tumors treated with siGFP/PEI, PEI, CD-PEI, and free siGFP (Fig. 7(a)). The decrease in green fluorescence signal was also observed in tumors treated with siGFP/CD-PEI excised from sacrificed mice. The red fluorescence in Cy5-siGFP-treated tumors totally disappeared due to degradation and removal of Cy5-siGFP. However, the Cy5 fluorescence signal from the Cy5-siGFP/CD-PEI treated tumor partially remained (Fig. 7(b)).

We next investigated the biodistribution of CD-PEI

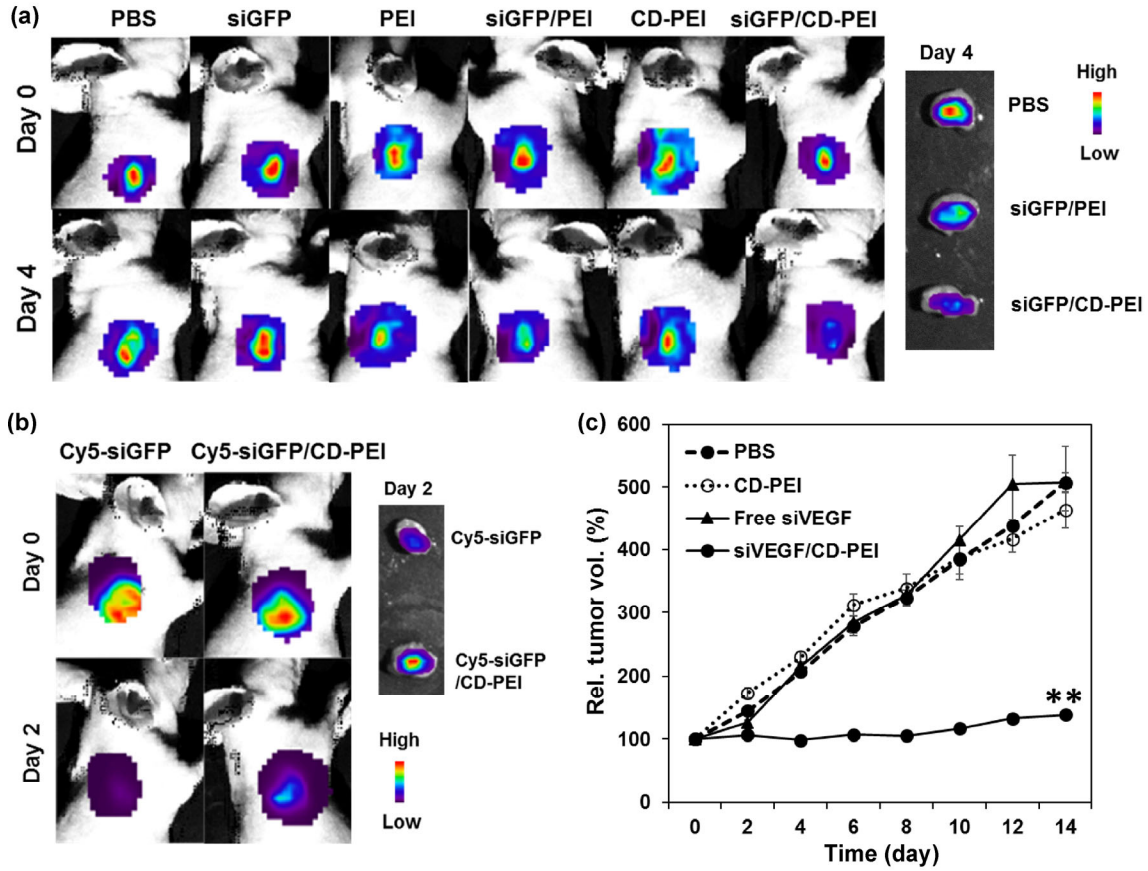

Figure 7 GFP knockdown and tumor growth inhibition *in vivo*. (a) Green fluorescence was monitored from tumors in GFP-HeLa xenograft-bearing mice. Significant decreases in GFP fluorescence were observed in the siGFP/CD-PEI-treated tumors compared to those treated with siGFP/PEI and free siGFP. (b) Red fluorescence originating from cy5-siGFP was observed in tumors. The Cy5 fluorescence from free Cy5-siGFP-treated tumors totally disappeared due to degradation and removal of Cy5-siGFP, whereas the corresponding signal from the Cy5-siGFP/CD-PEI treated tumor was notably high. (c) Relative tumor volumes measured over 14 days after the MDA-MB-231 tumor-bearing mice were treated with PBS, CD-PEI, free siVEGF, and siVEGF/CD-PEI intravenously three times (0, 5, and 10 days). *P*-values were calculated by student's *t*-test, ** for $P < 0.01$, $n = 4$.

following systemic administration with consideration for further *in vivo* applications. Fluorescence from CD-PEI was monitored in HeLa tumor-bearing xenograft mice by whole body imaging, and then major organs were excised from the mice. The fluorescence signals corresponding to CD-PEI were strongly observed in tumor and slightly visible in intestine, liver, and spleen, showing the correlation of the distribution of NPs [61–63] and tumor-specific accumulation (Fig. S11 in the ESM). It is well known that drug carriers in a size range from 10 to 100 nm are allowed to escape from the circulation owing to the inherent leakiness and the enhanced permeability of the underdeveloped tumor vasculature [64]. Our siRNA delivery system took advantage of the enhanced permeability and retention (EPR) effect due to well-suited size distribution of the siRNA/CD-PEI complex (Fig. 4(b) and Fig. S2(c) in the ESM).

Finally, we investigated the anti-tumor capability of the siRNA/CD-PEI complex against human cancer xenograft via IV injection of siVEGF/CD-PEI complexes. Each tumor was generated and grown to 60 mm^3 in volume, then treated with CD-PEI, free siVEGF, siVEGF/CD-PEI, and 1× PBS by IV injection. The changes in tumor volume in each group were monitored for 14 days and the relative tumor volumes were measured by comparing to the initial volumes. As shown in Fig. 7(c), tumor growth in the siVEGF/CD-PEI-treated group was significantly inhibited. However, the mice treated with CD-PEI only and free

siVEGF showed no notable difference in tumor size compared to the control 1× PBS-treated group, supporting the theory that anti-tumor activity through RNAi was strongly enhanced by CD-PEI-mediated siRNA delivery without any deleterious effect from CD-PEI itself, and protective effects of CD-PEI against degradation of the siRNA. A statistically significant difference was shown between the tumors in the siVEGF/CD-PEI-treated group and those of the other groups. Taken together, our CD-PEI-mediated functional siRNA delivery system was successfully demonstrated in an *in vivo* mouse model, showing the remarkable gene knockdown efficacy and siRNA protection from degradation *in vivo*.

4 Conclusion

In this study, we developed an efficient siRNA delivery system using CD-PEI and demonstrated that the siRNA/CD-PEI complex was successfully harnessed to knock down GFP and VEGF gene expression *in vitro* and *in vivo*. In addition, the intracellular distribution of CD-PEI with siRNA was monitored based on the intrinsic intense fluorescence of CD-PEI over time. The present CD-PEI-based siRNA delivery system possesses many advantages for biomedical applications. First, this strategy is technically simple to prepare because CD-PEI is directly synthesized from a mixture of citric acid and PEI using a household microwave and the reaction time is only 2 min. Second, CD-PEI simultaneously enabled both efficient target gene silencing by delivering siRNA into cells and convenient intracellular tracking of the gene delivery vehicle based on the fluorescence of CD-PEI itself without requiring conjugation of fluorescent dyes to the nanoparticle. In the present study, PEI played multiple important roles, as a carbon source with citric acid for CD formation in addition to surface passivation agent to enhance CD fluorescence, and as a condensing layer for siRNA.

Although several approaches to drug delivery systems using CD NPs were reported, systemic introduction of the CD therapeutic complex *in vivo* for tumor-specific treatment has remained a challenge until now. In this regard, the present work is the first demonstration of a CD-based RNAi approach, both *in vitro* and *in vivo*, with high gene knockdown efficacy and biomolecular imaging capability achieved by systemic intravenous administration. We expect that the present siRNA delivery platform will be a useful addition to current siRNA delivery systems, enabling highly effective and modular gene silencing with simultaneous bioimaging capability. In addition, due to its relatively low cytotoxicity and immunostimulatory properties, the CD-PEI-based siRNA delivery strategy can be readily applicable for gene therapy in the near future.

Acknowledgements

This work was supported by the Basic Science Research Program (Nos. 2011-0017356 and 2011-0020322), International S&T Cooperation Program (No. 2014K1B1A1073716) and the Research Center Program (No. IBS-R008-D1) of IBS (Institute for Basic Science) through the National Research Foundation of Korea (NRF) funded by the Korean government (MEST).

Electronic Supplementary Material: Supplementary material (further details of characteristic of CDs, confocal images, cell viability, PAGE analysis, and *in vivo* experiments) is available in the online version of this article at http://dx.doi.org/10.1007/s12274-016-1309-1.

References

[1] Hamilton, A. J.; Baulcombe, D. C. A species of small antisense RNA in posttranscriptional gene silencing in plants. *Science* **1999**, *286*, 950–952.

[2] Elbashir, S. M.; Harborth, J.; Lendeckel, W.; Yalcin, A.; Weber, K.; Tuschl, T. Duplexes of 21-nucleotide RNAs mediate RNA interference in cultured mammalian cells. *Nature* **2001**, *411*, 494–498.

[3] Fire, A.; Xu, S. Q.; Montgomery, M. K.; Kostas, S. A.; Driver, S. E.; Mello, C. C. Potent and specific genetic interference by double-stranded RNA in *Caenorhabditis elegans*. *Nature* **1998**, *391*, 806–811.

[4] Nykänen, A.; Haley, B.; Zamore, P. D. ATP requirements and small interfering RNA structure in the RNA interference pathway. *Cell* **2001**, *107*, 309–321.

[5] Martinez, J.; Patkaniowska, A.; Urlaub, H.; Lührmann, R.; Tuschl, T. Single-stranded antisense siRNAs guide target

RNA cleavage in RNAi. *Cell* **2002**, *110*, 563–574.

[6] Dorsett, T.; Tuschl, T. siRNAs: Applications in functional genomics and potential as therapeutics. *Nat. Rev. Drug Discov.* **2004**, *3*, 318–329.

[7] Djiane, A.; Yogev, S.; Mlodzik, M. The apical determinants aPKC and dPatj regulate frizzled-dependent planar cell polarity in the *Drosophila* eye. *Cell* **2005**, *121*, 621–631.

[8] Bumcrot, D.; Manoharan, M.; Koteliansky, V.; Sah, D. W. RNAi therapeutics: A potential new class of pharmaceutical drugs. *Nat. Chem. Biol.* **2006**, *2*, 711–719.

[9] Soutschek, J.; Akinc, A.; Bramlage, B.; Charisse, K.; Constien, R.; Donoghue, M.; Elbashir, S.; Geick, A.; Hadwiger, P.; Harborth, J. et al. Therapeutic silencing of an endogenous gene by systemic administration of modified siRNAs. *Nature* **2004**, *432*, 173–178.

[10] Dykxhoorn, D. M.; Palliser, D.; Lieberman, J. The silent treatment: siRNAs as small molecule drugs. *Gene Ther.* **2006**, *13*, 541–552.

[11] Dykxhoorn, D. M.; Lieberman, J. Running interference: Prospects and obstacles to using small interfering RNAs as small molecule drugs. *Annu. Rev. Biomed. Eng.* **2006**, *8*, 377–402.

[12] Whitehead, K. A.; Langer, R.; Anderson, D. G. Knocking down barriers: Advances in siRNA delivery. *Nat. Rev. Drug Discov.* **2009**, *8*, 129–138.

[13] Niikura, K.; Kobayashi, K.; Takeuchi, C.; Fujitani, N.; Takahara, S.; Ninomiya, T.; Hagiwara, K.; Mitomo, H.; Ito, Y.; Osada, Y. et al. Amphiphilic gold nanoparticles displaying flexible bifurcated ligands as a carrier for siRNA delivery into the cell cytosol. *ACS Appl. Mater. Interfaces* **2014**, *6*, 22146–22154.

[14] Zheng, D.; Giljohann, D. A.; Chen, D. L.; Massich, M. D.; Wang, X. Q.; Iordanov, H.; Mirkin, C. A.; Paller, A. S. Topical delivery of siRNA-based spherical nucleic acid nanoparticle conjugates for gene regulation. *Proc. Natl. Acad. Sci. USA* **2012**, *109*, 11975–11980.

[15] Lee, J. H.; Lee, K.; Moon, S. H.; Lee, Y.; Park, T. G.; Cheon, J. All-in-one target-cell-specific magnetic nanoparticles for simultaneous molecular imaging and siRNA delivery. *Angew. Chem., Int. Ed.* **2009**, *48*, 4174–4179.

[16] Derfus, A. M.; Chen, A. A.; Min, D. H.; Ruoslahti, E.; Bhatia, S. N. Targeted quantum dot conjugates for siRNA delivery. *Bioconjugate Chem.* **2007**, *18*, 1391–1396.

[17] Lee, H.; Kim, I. K.; Park, T. G. Intracellular trafficking and unpacking of siRNA/quantum dot-PEI complexes modified with and without cell penetrating peptide: Confocal and flow cytometric FRET analysis. *Bioconjugate Chem.* **2010**, *21*, 289–295.

[18] Na, H. K.; Kim, M. H.; Park, K.; Ryoo, S. R.; Lee, K. E.; Jeon, H.; Ryoo, R.; Hyeon, C.; Min, D. H. Efficient functional delivery of siRNA using mesoporous silica nanoparticles with ultralarge pores. *Small* **2012**, *8*, 1752–1761.

[19] Urban-Klein, B.; Werth, S.; Abuharbeid, S.; Czubayko, F.; Aigner, A. RNAi-mediated gene-targeting through systemic application of polyethylenimine (PEI)-complexed siRNA *in vivo*. *Gene Ther.* **2005**, *12*, 461–466.

[20] Yano, J.; Hirabayashi, K.; Nakagawa, S.; Yamaguchi, T.; Nogawa, M.; Kashimori, I.; Naito, H.; Kitagawa, H.; Ishiyama, K.; Ohgi, T. et al. Antitumor activity of small interfering RNA/cationic liposome complex in mouse models of cancer. *Clin. Cancer Res.* **2004**, *10*, 7721–7726.

[21] Sun, C. Y.; Shen, S.; Xu, C. F.; Li, H. J.; Liu, Y.; Cao, Z. T.; Yang, X. Z.; Xia, J. X.; Wang, J. Tumor acidity-sensitive polymeric vector for active targeted siRNA delivery. *J. Am. Soc. Chem.* **2015**, *137*, 15217–15224.

[22] Ngamcherdtrakul, W.; Morry, J.; Gu, S. D.; Castro, D. J.; Goodyear, S. M.; Sangvanich, T.; Reda, M. M.; Lee, R.; Mihelic, S. A.; Beckman, B. L. et al. Cationic polymer modified mesoporous Silica nanoparticles for targeted siRNA delivery to $HER2^+$ breast cancer. *Adv. Funct. Mater.* **2015**, *25*, 2646–2659.

[23] Lv, H. T.; Zhang, S. B.; Wang, B.; Cui, S. H.; Yan, J. Toxicity of cationic lipids and cationic polymers in gene delivery. *J. Control. Release* **2006**, *114*, 100–109.

[24] Yang, S. T.; Cao, L.; Luo, P. G.; Lu, F. S.; Wang, X.; Wang, H. F.; Meziani, M. J.; Liu, Y. F.; Qi, G.; Sun, Y. P. Carbon dots for optical imaging *in vivo*. *J. Am. Chem. Soc.* **2009**, *131*, 11308–11309.

[25] Baker, S. N.; Baker, G. A. Luminescent carbon nanodots: Emergent nanolights. *Angew. Chem., Int. Ed.* **2010**, *49*, 6726–6744.

[26] Liu, C. J.; Zhang, P.; Tian, F.; Li, W. C.; Li, F.; Liu, W. G. One-step synthesis of surface passivated carbon nanodots by microwave assisted pyrolysis for enhanced multicolor photoluminescence and bioimaging. *J. Mater. Chem.* **2011**, *21*, 13163–13167.

[27] Li, H. T.; Kang, Z. H.; Liu, Y.; Lee, S. T. Carbon nanodots: Synthesis, properties and applications. *J. Mater. Chem.* **2012**, *22*, 24230–24253.

[28] Zhai, X. Y.; Zhang, P.; Liu, C. J.; Bai, T.; Li, W. C.; Dai, L. M.; Liu, W. G. Highly luminescent carbon nanodots by microwave-assisted pyrolysis. *Chem. Commun.* **2012**, *48*, 7955–7957.

[29] Miao, P.; Han, K.; Tang, Y. G.; Wang, B. D.; Lin, T.; Cheng, W. B. Recent advances in carbon nanodots: Synthesis, properties and biomedical applications. *Nanoscale* **2015**, *7*, 1586–1595.

[30] Zheng, X. T.; Ananthanarayanan, A.; Luo, K. Q.; Chen, P. Glowing graphene quantum dots and carbon dots: Properties, syntheses, and biological applications. *Small* **2015**, *11*, 1620–1636.

[31] Zhang, T. Q.; Liu, X. Y.; Fan, Y.; Guo, X. Y.; Zhou, L.; Lv, Y.; Lin, J. One-step microwave synthesis of N-doped hydroxyl-functionalized carbon dots with ultra-high fluorescence quantum yields. *Nanoscale* **2016**, *8*, 15281–15287.

[32] Tang, J.; Kong, B.; Wu, H.; Xu, M.; Wang, Y. C.; Wang, Y. L.; Zhao, D. Y.; Zheng, G. F. Carbon nanodots featuring efficient FRET for real-time monitoring of drug delivery and two-photon imaging. *Adv. Mater.* **2013**, *25*, 6569–6574.

[33] Liu, C. J.; Zhang, P.; Zhai, X. Y.; Tian, F.; Li, W. C.; Yang, J. H.; Liu, Y.; Wang, H. B.; Wang, W.; Liu, W. G. Nano-carrier for gene delivery and bioimaging based on carbon dots with PEI-passivation enhanced fluorescence. *Biomaterials* **2012**, *33*, 3604–3613.

[34] Hu, L. M.; Sun, Y.; Li, S. L.; Wang, X. L.; Hu, K. L.; Wang, L. R.; Liang, X. J.; Wu, Y. Multifunctional carbon dots with high quantum yield for imaging and gene delivery. *Carbon* **2014**, *67*, 508–513.

[35] Cao, L.; Wang, X.; Meziani, M. J.; Lu, F. S.; Wang, H. F.; Luo, P. G.; Lin, Y.; Harruff, B. A.; Veca, L. M.; Murray, D. et al. Carbon dots for multiphoton bioimaging. *J. Am. Chem. Soc.* **2007**, *129*, 11318–11319.

[36] Zhu, S. J.; Meng, Q. N.; Wang, L.; Zhang, J. H.; Song, Y. B.; Jin, H.; Zhang, K.; Sun, H. C.; Wang, H. Y.; Yang, B. Highly photoluminescent carbon dots for multicolor patterning, sensors, and bioimaging. *Angew. Chem., Int. Ed.* **2013**, *52*, 3953–3957.

[37] Zhu, A. W.; Qu, Q.; Shao, X. L.; Kong, B.; Tian, Y. Carbon-dot-based dual-emission nanohybrid produces a ratiometric fluorescent sensor for *in vivo* imaging of cellular copper ions. *Angew. Chem., Int. Ed.* **2012**, *51*, 7185–7189.

[38] Huang, P.; Lin, J.; Wang, X. S.; Wang, Z.; Zhang, C. L.; He, M.; Wang, K.; Chen, F.; Li, Z. M.; Shen, G. X. et al. Light-triggered theranostics based on photosensitizer-conjugated carbon dots for simultaneous enhanced-fluorescence imaging and photodynamic therapy. *Adv. Mater.* **2012**, *24*, 5104–5110.

[39] Hola, K.; Zhang, Y.; Wang, Y.; Giannelis, E. P.; Zboril, R.; Rogach, A. L. Carbon dots—Emerging light emitters for bioimaging, cancer therapy and optoelectronics. *Nano Today* **2014**, *9*, 590–603.

[40] Chen, D. Q.; Dougherty, C. A.; Zhu, K. C.; Hong, H. Theranostic applications of carbon nanomaterials in cancer: Focus on imaging and cargo delivery. *J. Control. Release* **2015**, *210*, 230–245.

[41] Dong, Y. Q.; Wang, R. X.; Li, H.; Shao, J. W.; Chi, Y. W.; Lin, X. M.; Chen, G. N. Polyamine-functionalized carbon quantum dots for chemical sensing. *Carbon* **2012**, *50*, 2810–2815.

[42] Yu, P.; Wen, X. M.; Toh, Y. R.; Tang, J. Temperature-dependent fluorescence in carbon dots. *J. Phys. Chem. C* **2012**, *116*, 25552–25557.

[43] Mei, Q. S.; Zhang, K.; Guan, G. J.; Liu, B. H.; Wang, S. H.; Zhang, Z. P. Highly efficient photoluminescent graphene oxide with tunable surface properties. *Chem. Commun.* **2010**, *46*, 7319–7321.

[44] Kim, H.; Kim, W. J. Photothermally controlled gene delivery by reduced graphene oxide-polyethylenimine nanocomposite. *Small* **2014**, *10*, 117–126.

[45] Dong, Y. Q.; Pang, H. C.; Yang, H. B.; Guo, C. X.; Shao, J. W.; Chi, Y. W.; Li, C. M.; Yu, T. Carbon-based dots co-doped with nitrogen and sulfur for high quantum yield and excitation-independent emission. *Angew. Chem., Int. Ed.* **2013**, *52*, 7800–7804.

[46] Singha, K.; Namgung, R.; Kim, W. J. Polymers in small-interfering RNA delivery. *Nucleic Acid Ther.* **2011**, *21*, 133–147.

[47] Bieber, T.; Elsässer, H. P. Preparation of a low molecular weight polyethylenimine for efficient cell transfection. *Biotechniques* **2001**, *30*, 74–77, 80–81.

[48] Gosselin, M. A.; Guo, W. J.; Lee, R. J. Efficient gene transfer using reversibly cross-linked low molecular weight polyethylenimine. *Bioconjugate Chem.* **2001**, *12*, 989–994.

[49] Hu, C.; Peng, Q.; Chen, F. J.; Zhong, Z. L.; Zhuo, R. X. Low molecular weight polyethylenimine conjugated gold nanoparticles as efficient gene vectors. *Bioconjugate Chem.* **2010**, *21*, 836–843.

[50] Nunes, A.; Amsharov, N.; Guo, C.; Van den Bossche, J.; Santhosh, P.; Karachalios, T. K.; Nitodas, S. F.; Burghard, M.; Kostarelos, K.; Al-Jamal, K. T. Hybrid polymer-grafted multiwalled carbon nanotubes for *in vitro* gene delivery. *Small* **2010**, *6*, 2281–2291.

[51] Boussif, O.; Lezoualc'h, F.; Zanta, M. A.; Mergny, M. D.; Scherman, D.; Demeneix, B.; Behr, J. P. A versatile vector for gene and oligonucleotide transfer into cells in culture and *in vivo*: Polyethylenimine. *Proc. Natl. Acad. Sci. USA* **1995**, *92*, 7297–7301.

[52] Fischer, D.; Bieber, T.; Li, Y. X.; Elsässer, H. P.; Kissel, T. A novel non-viral vector for DNA delivery based on low molecular weight, branched polyethylenimine: Effect of molecular weight on transfection efficiency and cytotoxicity. *Pharm. Res.* **1999**, *16*, 1273–1279.

[53] Sharma, V. K.; Thomas, M.; Klibanov, A. M. Mechanistic studies on aggregation of polyethylenimine-DNA complexes and its prevention. *Biotechnol. Bioeng.* **2005**, *90*, 614–620.

[54] Wang, X. L.; Zhou, L. Z.; Ma, Y. J.; Li, X.; Gu, H. C. Control of aggregate size of polyethyleneimine-coated magnetic nanoparticles for magnetofection. *Nano Res.* **2009**, *2*, 365–372.

[55] Chen, H. H.; Ho, Y. P.; Jiang, X.; Mao, H. Q.; Wang, T. H.; Leong, K. W. Quantitative comparison of intracellular unpacking kinetics of polyplexes by a model constructed from quantum dot-FRET. *Mol. Ther.* **2008**, *16*, 324–332.

[56] Ferrara, N. The role of vascular endothelial growth factor in pathological angiogenesis. *Breast Cancer Res. Treat.* **1995**, *36*, 127–137.

[57] Takei, Y.; Kadomatsu, K.; Yuzawa, Y.; Matsuo, S.; Muramatsu, T. A small interfering RNA targeting vascular endothelial growth factor as cancer therapeutics. *Cancer Res.* **2004**, *64*, 3365–3370.

[58] Alexopoulou, L.; Holt, A. C.; Medzhitov, R.; Flavell, R. A. Recognition of double-stranded RNA and activation of NF-κB by Toll-like receptor 3. *Nature* **2001**, *413*, 732–738.

[59] Matsumoto, M.; Seya, T. TLR3: Interferon induction by double-stranded RNA including poly(I: C). *Adv. Drug Deliv. Rev.* **2008**, *60*, 805–812.

[60] Ryoo, S. R.; Jang, H.; Kim, K. S.; Lee, B.; Kim, K. B.; Kim, Y. K.; Yeo, W. S.; Lee, Y.; Kim, D. E.; Min, D. H. Functional delivery of DNAzyme with iron oxide nanoparticles for hepatitis C virus gene knockdown. *Biomaterials* **2012**, *33*, 2754–2761.

[61] Lammers, T.; Peschke, P.; Kühnlein, R.; Subr, V.; Ulbrich, K.; Huber, P.; Hennink, W.; Storm, G. Effect of intratumoral injection on the biodistribution, the therapeutic potential of HPMA copolymer-based drug delivery systems. *Neoplasia* **2006**, *8*, 788–795.

[62] Moon, H. K.; Lee, S. H.; Choi, H. C. *In vivo* near-infrared mediated tumor destruction by photothermal effect of carbon nanotubes. *ACS Nano* **2009**, *3*, 3707–3713.

[63] Almeida, J. P. M.; Chen, A. L.; Foster, A.; Drezek, R. *In vivo* biodistribution of nanoparticles. *Nanomedicine* **2011**, *6*, 815–835.

[64] Petros, R. A.; DeSimone, J. M. Strategies in the design of nanoparticles for therapeutic applications. *Nat. Rev. Drug Discov.* **2010**, *9*, 615–627.